Available online at www.sciencedirect.com

ScienceDirect

Underground Space 7 (2022) 1003–1020

www.keaipublishing.com/undsp

Role of plastic zone porosity and permeability in sand production in weak sandstone reservoirs

Ainash Shabdirova [a,*], Nguyen Hop Minh [b], Yong Zhao [a]

[a] School of Engineering and Digital Sciences, Nazarbayev University, Nur-Sultan, Kazakhstan
[b] Fulbright University Vietnam, Ho Chi Minh City, Viet Nam

Received 14 October 2020; received in revised form 13 September 2021; accepted 14 October 2021
Available online 6 May 2022

Abstract

Sand production is often characterized as a two-stage process, in which material failure occurs near the cavity, leading to the formation of a plastic zone, from which particles are detached and transported out because of continuous hydrodynamic erosion under the effects of the produced fluid flow. The plastic zone porosity is affected by coupled processes, while the plastic zone permeability has a significant impact on the performance of sand production prediction, especially in weak sandstone reservoirs. Large-scale sand production experiments were conducted using a customized high-pressure consolidation apparatus. The results show that specific stress-fluid pressure conditions may create a plastic zone around a hole, which has lower permeability than the intact zone. The plastic zone comprises two subzones: a high-permeability shear band zone and a low-permeability compaction zone. During sand production, sand migrates from the compaction zone through the shear band zone to the perforation hole. Thus, sand production is associated with the increased permeability and porosity in the compaction zone. Existing sand prediction models were modified according to the new findings, resulting in a modified model with improved performance. The modified model was validated using the sanding data from a weak sandstone reservoir in Kazakhstan.

Keywords: Sand production; Plastic zone; Weak sandstone; Porosity; Permeability

1 Introduction

Weak shallow oil reservoirs are prone to sand production that can lead to additional costs owing to equipment failure, well shutdown, and environmental contamination.

The sand production phenomenon can be considered as a two-stage process. First, the material around a borehole fails when stresses exceed the strength of the material. Second, the disaggregation and transportation of the failed material occur because of fluid flow.

The prediction of sanding onset involves formulating stress solutions near the hole and then applying failure criteria to these stresses, which requires a constitutive material model and failure criterion. Sanding onset conditions have been studied in detail and accurately predicted for most field cases (Al-Shaaibi et al., 2013; Araujo et al., 2014; Fuh & Morita, 2013; Han et al., 2011; Kessler et al., 1993; Morita et al., 2007; Papamichos & Furui, 2013, 2019; Wang & Dusseault, 1996; Weingarten & Perkins, 1995; Wu et al., 2006). The most commonly used material model to study sand production is the linear poroelastoplastic model (Al-Shaaibi, et al. 2013; Hayavi & Abdideh, 2017; Morita et al., 2007; Papamichos et al., 2001; Wang & Sharma, 2017; Yi, 2003). The model describes the mechanical behavior of porous media in terms of the applied effective stresses carried by the solid skeleton and the fluid inside the pores. When the applied effective stresses exceed the material strength, the material is expected to fail and change its state from elastic to plastic. A plastic deformation zone of the material forms around the cavity, and failure occurs when the shear failure criterion is

* Corresponding author.
E-mail address: ainash.shabdirova@nu.edu.kz (A. Shabdirova).

https://doi.org/10.1016/j.undsp.2021.10.005

Nomenclature

k	Intact zone permeability	R_p	Radius of plastic zone
k_0	Permeability coefficient	R_{sb}	Radius of shear band zone
k_{ave}	Average permeability of the sample	S_0	Inherent shear strength
k_c	Permeability of compaction zone	t	Time
k_p	Permeability of plastic zone	α	Failure angle
k_{sb}	Permeability of shear band zone	φ	Friction angle
L	Perforation length	ψ	Dilatancy angle
η	Viscoplastic viscosity	γ	Poroelastic coefficient
n	Proportionality coefficient	μ	Fluid viscosity
N	Number of perforations	v_{fr}	Drained Poisson's ratio
p_o	Fluid pressure at boundary	ρ_s	Density of sand grains
p_i	Fluid pressure at wellbore wall	σ_{1e}'	Effective maximum principal stress
p_p	Fluid pressure at plastic/elastic zones boundary	σ_{3p}'	Effective minimum principal stress
Δp	Drawdown	σ_h	Minimum horizontal stress
p'	The mean effective stress	σ_H	Maximum horizontal stress
q	Fluid flow rate	σ_r	Radial stress at distance r
q_p	Fluid flow rate across plastic zone	σ_v	Far-field vertical overburden stress
q_{avg}	Average fluid flow rate across the sample	σ_z	Axial stress at distance r
q	Deviatoric stress	σ_θ	Tangential stress
r	Radial distance from hole axis	ϕ	Porosity in the intact zone
R_i	Radius of perforation tunnel	ϕ_c	Porosity in the compaction zone
R_o	Radius of outer boundary for perforation tunnel	ϕ_p	Porosity in the plastic zone
R_c	Radius of compaction zone	ϕ_{sb}	Porosity in the shear band zone

satisfied in terms of the stress distribution in the plastic zone, which is dependent on the flow characteristics, i.e., fluid flow rate and rock permeability. The linear Mohr–Coulomb failure criterion states that shear failure is solely dependent on the minimum and maximum principal stresses (Fjaer et al., 2008):

$$\tau = S_0 + \mu\sigma', \tag{1}$$

where τ is the shear stress, S_0 is the cohesion, μ is the coefficient of internal friction, and $\sigma\prime$ is the normal stress.

Despite its simplicity, the Mohr–Coulomb criterion has been successfully employed to predict the onset of sanding in some fields (Hayavi & Abdideh, 2017; Yi, 2003).

When the stresses around a cavity increase and meet the failure criterion, the material state transforms from elasticity to plasticity. Bratli and Risnes (1981) identified the plastic zone of failed materials around a sand arch after a shear failure. First, the in situ stresses near the sand arch were calculated. The greatest difference between stresses occurred on the inner surface, and this region was the first one that failed. The material behaved elastically up to the limit set by the Mohr–Coulomb failure criterion. Risnes et al. (1982) extended this work by investigating the stresses around open borehole and cased-hole completions. Following these studies, the formation of plastic zones has been reported in several experimental and numerical studies (Goshtasbi et al., 2013; Tronvoll & Fjær, 1994; Wang & Sharma, 2017).

A literature review on plastic zone permeability showed limited and contradictory results, such as different values across the plastic zone in Bratli and Risnes (1981), and a single value that is one-tenth of the intact zone permeability in Risnes et al. (1982).

Permeability alteration in the near-borehole area can result from both the stress changes around the hole and the particle invasion during hole creation. Daigle et al. (2017) developed a numerical model of a depleted North Sea reservoir to show the permeability reduction in the near-wellbore area. They attributed this compaction to the increase in effective stresses in the reservoir.

Cuss et al. (2003) experimentally observed the porosity reduction near a borehole wall and borehole breakouts during hydrostatic loading due to stress concentration. Han and Dusseault (2003) analytically estimated the stress-dependent porosity and permeability in the plastic zone defined by the Mohr–Coulomb shear failure around a wellbore. They concluded that the reduction is negligible for unconsolidated sandstones, which contradicted the results of other experimental studies on the stress-dependent permeability of weak porous sandstones (Holt, 1990; Sarda et al., 1988), which found a permeability reduction of over 50%.

Zhu and Wong (1997) studied the transition from brittle failure to cataclastic flow. They found that for porous sandstones, the permeability decreased before the peak stress was reached. Tovar et al. (2007) described this

permeability reduction as geomechanical damage and introduced a methodology to quantify a skin factor due to the combined action of geomechanical damage and fluid invasion damage. On the contrary, weak rocks are characterized by a slip line breakout mode that forms high-permeability shear bands around a hole. Hollow cylinder experiments and numerical modeling conducted by Cerasi et al. (2005) showed that the shear bands did not extend throughout the entire plastic zone but were concentrated near the borehole.

Arora and Sharma (2000) developed a model to understand the factors controlling the permeability distribution around a perforated tunnel. They found that during underbalance perforating, the permeability around the perforation was controlled by fines both generated by the shock wave and transported during surge flow back into the wellbore. They identified the high-permeability region of the failed material near the perforation owing to the fractures. This region was followed by a compaction zone comprising crushed and squeezed sand particles.

A recent study by Khamitov et al. (2021) investigated sand production using the coupled discrete element method/computational fluid dynamics model. They determined the porosity distribution around the perforation hole with radius r, i.e., a high-porosity zone near the perforation tunnel at a radial distance between r and $2r$, and a low-porosity zone between $2r$ and $5r$.

A few controversial studies have been conducted on the properties of the plastic zone around a hole in weak sandstone. A sensitivity analysis of the sand volume prediction model for weak sandstone reservoirs in Kazakhstan by Shabdirova et al. (2019) suggested that the plastic zone permeability had a strong influence on the prediction. In this study, sand production experiments were conducted using a customized apparatus to investigate the porosity and permeability distributions in the plastic zone. The results were incorporated into existing sand prediction models (Papamichos et al., 2001; van den Hoek & Geilikman, 2003) to demonstrate the importance of plastic zone properties. The modified models were then used to predict the sanding data of an oil field in the Ustuyrt–Buzachi sedimentary basin in Kazakhstan. This study aims to demonstrate the significance of the plastic zone porosity and permeability distribution in sand production prediction. The novelty of this study is the modification of existing sand production models in terms of plastic zone permeability and porosity based on experimental data. The modified models were validated against the production data of 40 wells in the oil field. The efficiency of the models was proven, and appropriate modifications will be made based on more realistic assumptions.

2 Development of a sanding prediction model for weak sandstone reservoir

Following the concept of a two-stage process in sand production, the model was developed based on the assumption of a shear failure model, a flow model, an erosion model, and a material model.

2.1 Shear failure model for the formation of the plastic zone

An isotropic and homogenous cylindrical sample with a central through-hole was considered (Fig. 1), where R_i is the inner hole radius and R_o is the outer boundary radius.

A poroelastoplastic material model was employed to determine the stress distributions around the hole, which adequately represents weak porous formations in sand production studies (Al-Shaaibi et al., 2013; Hayavi & Abdideh, 2017; Morita et al., 2007; Papamichos et al., 2001; Wang & Sharma, 2017; Yi, 2003). The cylindrical geometry of a perforation tunnel is presented in Fig. 1, with an outer boundary radius R_o and an inner hole radius R_i. The stresses in the intact zone can be expressed as follows (Risnes et al., 1982):

$$\sigma_r = \sigma_h + (\sigma_h - p_i)\frac{R_i^2}{R_o^2 - R_i^2}\left[1 - \frac{R_o^2}{r^2}\right] - (p_o - p_i)\eta\left\{\frac{R_i^2}{R_o^2 - R_i^2}\left[1 - \frac{R_o^2}{r^2}\right] + \frac{\ln\frac{R_o}{r}}{\ln\frac{R_o}{R_i}}\right\}, \quad (2)$$

$$\sigma_\theta = \sigma_h + (\sigma_h - p_i)\frac{R_i^2}{R_o^2 - R_i^2}\left[1 + \frac{R_o^2}{r^2}\right] - (p_o - p_i)\eta\left\{\frac{R_i^2}{R_o^2 - R_i^2}\left[1 + \frac{R_o^2}{r^2}\right] + \frac{\ln\frac{R_o}{r} - 1}{\ln\frac{R_o}{R_i}}\right\}, \quad (3)$$

$$\sigma_z = \sigma_v + 2\nu_{fr}(\sigma_h - p_i)\frac{R_i^2}{R_o^2 - R_i^2} - (p_o - p_i)\eta\left\{\frac{2\nu_{fr}R_i^2}{R_o^2 - R_i^2} + \frac{2\ln\frac{R_o}{r} - \nu_{fr}}{\ln\frac{R_o}{R_i}}\right\}, \quad (4)$$

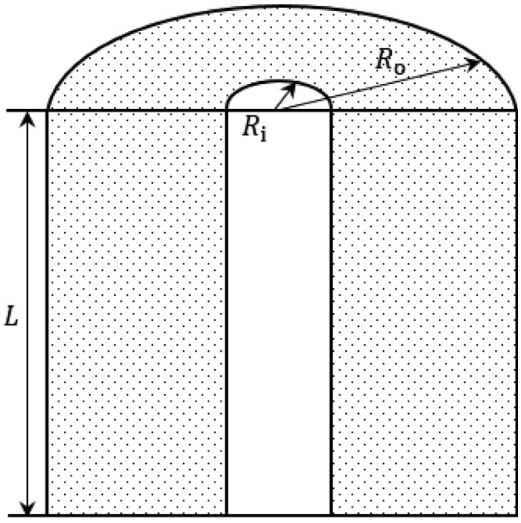

Fig. 1. Cylindrical sample with a central hole.

where σ_r is the radial stress at distance r from the hole axis, σ_h is the far-field minimum horizontal stress, p_i is the fluid pressure on the hole wall, R_i is the inner radius, R_o is the outer radius of the boundary, p_o is the fluid pressure at the outer boundary, η is the compressibility constant, σ_θ is the tangential stress at distance r from the perforation axis, v_{fr} is the Poisson's ratio, σ_z is the axial stress at distance r from the perforation axis, and σ_v is the far-field vertical stress. The far-field stresses are assumed to be the same in Eqs. (2)–(4).

The plastic zone around the perforation is formed when the stresses satisfy a shear failure condition according to the Mohr–Coulomb criterion. The stresses in the plastic zone are given as follows in Risnes et al. (1982):

$$\sigma_r = p_i + \frac{\mu q}{2\pi L k_p}\ln\left(\frac{r}{R_i}\right) + \frac{1}{\lambda_{tt}}\left(2S_0\tan\alpha - \frac{\mu q}{2\pi L k_p}\right)\left[\left(\frac{r}{R_i}\right)^{\lambda_{tt}} - 1\right], \quad (5)$$

$$\sigma_\theta = p_i + \frac{\mu q}{2\pi L k_p}\left(1 + \ln\left(\frac{r}{R_i}\right)\right) + \frac{1}{\lambda_{tt}}\left(2S_0\tan\alpha - \frac{\mu q}{2\pi L k_p}\right)\left[(\lambda_{tt}+1)\left(\frac{r}{R_i}\right)^{\lambda_{tt}} - 1\right], \quad (6)$$

$$\sigma_z = [2v_{fr}(1-\beta)+\beta]\left(p_i + \frac{\mu q}{2\pi L k_p}\ln\left(\frac{r}{R_i}\right)\right) + v_{fr}\frac{\mu q}{2\pi L k_p} + \frac{(1+v_{fr})(1-2v_{fr})}{1-v_{fr}}(\sigma_{zo} - \beta p_o) + \frac{v_{fr}}{t}\left[2S_0\tan\alpha - \frac{\mu q}{2\pi L k_p}\right]\left[(\lambda_{tt}+2)\left(\frac{r}{R_i}\right)^{\lambda_{tt}} - 2\right], \quad (7)$$

where q is the flow rate in the radial direction, μ is the fluid viscosity, L is the perforation length, k_p is the permeability of the plastic zone, α is the failure angle, S_0 is the inherent shear strength, β is the poroelastic constant, and $\lambda_{tt} = \tan^2\alpha - 1$.

The radius of the plastic zone can be determined when the stress distributions inside the intact zone and plastic zone satisfy the Mohr–Coulomb criterion at the interface between the two zones, which can be described in terms of the tangential principal stress in the intact zone (σ'_{1e}) and the radial principal stress in the plastic zone (σ'_{3p}) in Eq. (8). The plastic zone radius R_p can be obtained by knowing the stress values, flow rate, and plastic zone permeability k_p.

$$\sigma'_{1e} = 2S_0\tan\alpha + \sigma'_{3p}\tan^2\alpha, \quad (8)$$

where σ'_{1e} is the maximum principal stress in the intact zone, and σ'_{3p} is the minimum principal stress in the plastic zone. Note that while Eq. (8) allows the determination of R_p, the calculation requires knowledge of the plastic zone permeability k_p, which can be determined from the flow model in the following section.

2.2 Flow model across the intact zone and plastic zone

If we assume that the applied stresses and fluid pressures result in the formation of a plastic zone around a hole with the yet unknown radius and permeability, the cylindrical sample will appear, as shown in Fig. 2.

The plastic zone permeability k_p and the plastic zone radius R_p can be related to the intact zone permeability k, inner radius R_i, and outer boundary radius R_o by the average permeability of the sample k_{avg}. The radial flow was considered through a sample with two layers of varying permeabilities of the plastic and intact zones (Fig. 2).

The plastic zone permeability for flow in series can be expressed as follows (Fanchi, 2000):

$$k_p = \frac{k_{avg}k\ln\frac{R_p}{R_i}}{k\ln\frac{R_o}{R_i} - k_{avg}\ln\frac{R_o}{R_p}}. \quad (9)$$

The average permeability k_{avg} was determined from a radial flow experiment on a hollow cylinder sample similar to the geometry in Fig. 2 using Darcy's law, knowing the values of the applied drawdown ($\Delta p = p_o - p_i$) and the measured fluid flow rate (Dake, 2008), which is expressed as

$$k_{avg} = \frac{q\mu\ln\frac{R_o}{R_i}}{2\pi L\Delta p}. \quad (10)$$

Knowing the value of k_{avg} allows us to calculate the plastic zone permeability k_p in Eq. (9), which allows us to calculate R_p from the shear failure model in Eq. (8).

The hole failure mode in weak sandstones is characterized by the formation of shear bands (Wu & Choi, 2012; Wu et al., 2016; Yan et al., 2020). We propose that the shear band formation is accompanied by squeezing of the sample material behind the shear bands outward to the sample periphery owing to stress redistribution. Thus, there is a low-permeability compaction zone right after the high-permeability shear band zone. This proposition is supported by several other studies (Arora & Sharma, 2000; Khamitov et al., 2021).

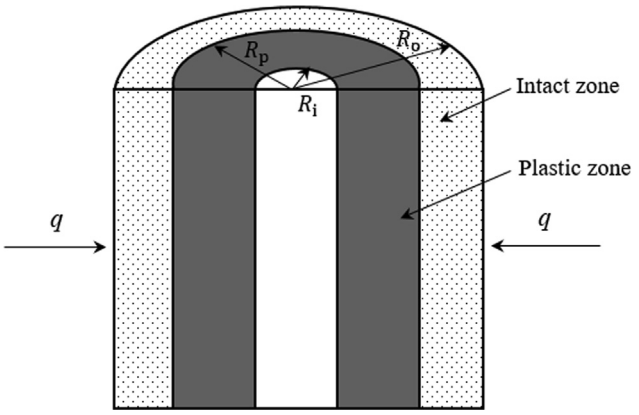

Fig. 2. The plastic zone around the hole in the cylindrical sample.

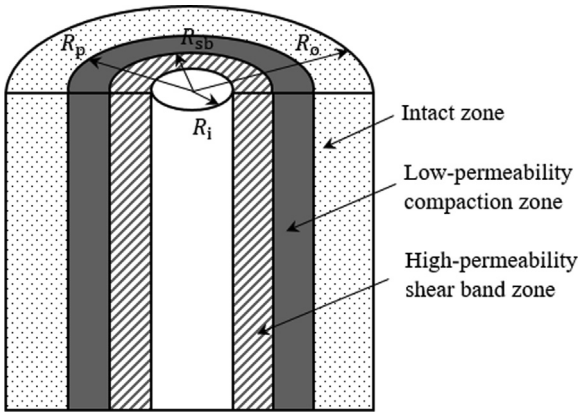

Fig. 3. Shear band zone and low-permeability compaction zone.

Following our approach, the cylindrical sample in Fig. 2 can be modified as shown in Fig. 3 to capture the new zone.

If we follow the idea of fluid flow across the plastic and intact zones presented above, then the average permeability of the sample in the case of radial flow can be written as (Fanchi, 2000)

$$k_{avg} = \frac{\ln \frac{R_o}{R_i}}{\frac{\ln \frac{R_{sb}}{R_i}}{k_{sb}} + \frac{\ln \frac{R_p}{R_{sb}}}{k_c} + \frac{\ln \frac{R_o}{R_p}}{k}}, \tag{11}$$

where R_{sb} is the radius of the shear band zone, R_p is the plastic zone radius, k_{sb} is the shear band zone permeability, and k_c is the compaction zone permeability.

Thus, the shear band zone with a width of $(R_{sb} - R_i)$ has a high permeability, while the compaction zone with a width of $(R_p - R_{sb})$ has a low permeability. As a result, the average permeability of the sample decreased compared with the intact permeability. A change in the flow rate redistributed the stresses and altered the radius and permeability in the shear band and compaction zones, which in turn changed the average permeability. Knowledge of the properties of these zones is important to estimate sand production.

Based on the above observations and discussions in the literature on stress-induced compaction (Cuss et al., 2003; Han et al., 2002; Holt, 1990; Raghavan & Chin, 1982; Sarda et al., 1988; Zhu & Wong, 1997) and shear bands around a hole in weak rocks (Arora & Sharma, 2000; Khamitov et al., 2021; Papamichos et al., 2000; Wu & Choi, 2012; Wu et al., 2016; Yan et al., 2020), we propose the following evolution of the plastic zone around a hole, depending on the applied stresses and fluid pressures. In the beginning, right after hole creation, a compaction zone (Fig. 4(a)) exists around the hole owing to the stress redistribution and the invasion of broken particles. The thickness, permeability, and porosity of this zone are dependent on the applied stresses and penetration method. Further stress conditions create shear bands and move the compaction front away from the hole (Fig. 4(b)). The properties of the shear bands and compaction zones may change with the stress conditions (Fig. 4(c)).

The introduction of fluid flow may enlarge the plastic zone and its further compaction until a critical value is reached. Once the fluid flow rate exceeds this value, sand particles begin to migrate from the compaction zone to the shear band zone and perforation hole. To provide a better understanding, the above discussions are illustrated in terms of the porosity change in different zones. We assumed a linear relationship between the porosity ϕ and permeability k given by the Kozeny–Carman equation (Carman, 1939; Kozeny, 1927):

$$k = k_0 \frac{\phi^3}{(1-\phi)^2}, \tag{12}$$

where k_0 is the permeability constant that accounts for the effects of the particle size and tortuosity of the sample.

Let us consider the conditions right before the initiation of sand production. For simplicity, we divided the plastic zone into two zones of equal size; however, the dimensions of these zones may be different. The first zone is a shear band zone, while the second is a compaction zone. If we superimpose the cross-section of a quarter of the cylindri-

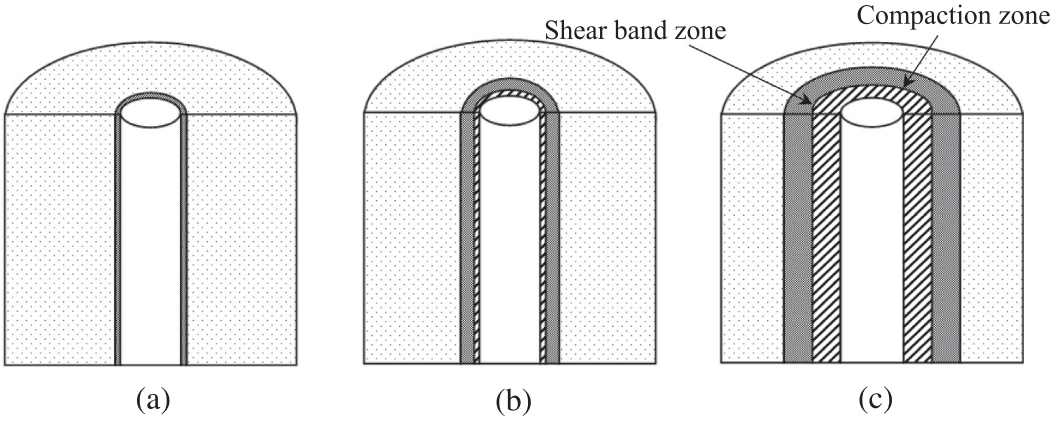

Fig. 4. Shear band and compaction zones around a hole: (a) right after hole creation, only compaction zone; (b) a shear band zone is formed and the compaction zone moves; and (c) zone properties change with the stress conditions.

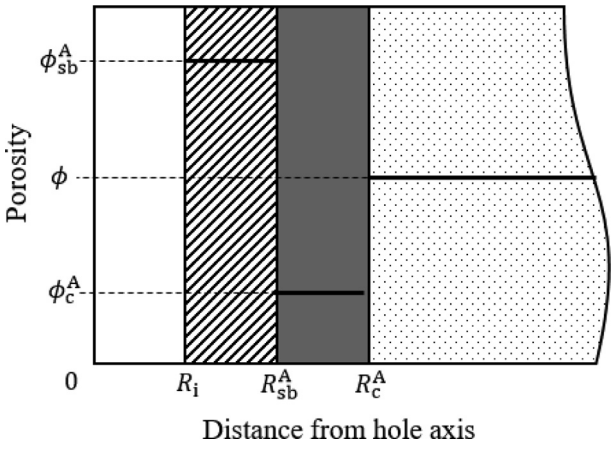

Fig. 5. Subzones of the plastic zone with different porosities before sand production.

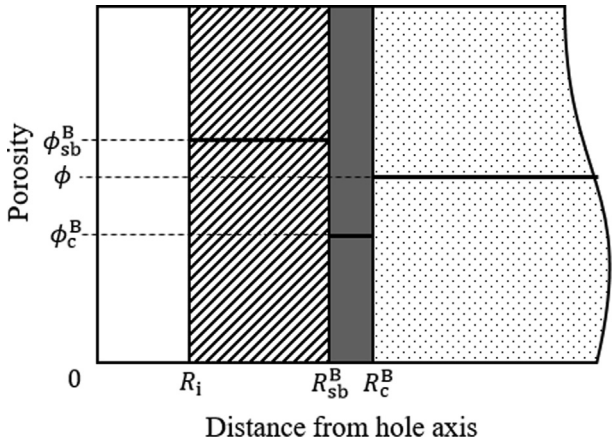

Fig. 6. Subzones of the plastic zone after sand production.

cal sample on the porosity vs. distance graph, we can illustrate the high-permeability shear band zone, low-permeability compaction zone, and intact zone (Fig. 5) in state A before sand production.

When the fluid rate exceeded a critical value, sand particles were detached from the compaction zone and transported to the shear band zone and perforation hole. This means that the porosity in the compaction zone increased because of the particles moving out, while the porosity in the shear band zone decreased because of the particles moving in. Note that the radii of the subzones also changed with the increase in flow rate.

Figure 6 shows one possible porosity change scenario after sand production. To simplify the calculations, this scenario will be used to estimate the porosity distribution during the sand production experiments. We can see that the shear band zone increased and the compaction zone moved away from the hole. The porosity in the shear band zone may decrease owing to sand migration, while the porosity in the compaction zone may increase owing to sand production. The compaction zone in state A was transformed into a shear band zone in state B. Superscripts A and B denote before sand production and after sand production, respectively.

k_p is the average permeability across the plastic zone; hence, analogous to the flow model above, we can write the following equation:

$$k_p = \frac{\ln\frac{R_p}{R_i}}{\frac{\ln\frac{R_{sb}}{R_i}}{k_{sb}} + \frac{\ln\frac{R_p}{R_{sb}}}{k_c}}. \tag{13}$$

For state A, if we assume that all the excess sand masses in the compacted zone are squeezed out of the shear band zone, we can write the mass balance equation as

$$m_{sb} = m_c. \tag{14}$$

For state B, a portion of the excess sand masses migrate from the compaction zone and produce

$$m_{sb} = m_c + m. \tag{15}$$

Here,

$$m_{sb} = \pi L\left(R_{sb}^2 - R_i^2\right)(\phi_{sb} - \phi)\rho, \tag{16}$$

$$m_c = \pi L\left(R_p^2 - R_{sb}^2\right)(\phi - \phi_c)\rho, \tag{17}$$

where m_{sb} is the sand mass squeezed from the shear band zone to the compaction zone, m_c is the sand mass squeezed into the compaction zone, m is the mass of the produced sand, L is the sample height, R_{sb} and R_p are the radii of the shear band and the plastic zones, respectively, ρ is the sand particle density, and ϕ, ϕ_{sb}, and ϕ_c are the porosity values of the intact zone, shear band zone, and compaction zone, respectively. These porosity values can be expressed in terms of the corresponding permeability values according to the Kozeny–Carman equation:

Fig. 7. High-pressure consolidation system.

$$\phi_{sb}=\frac{k_{sb}}{3k_0}+\sqrt[3]{\left(\frac{1}{27}\cdot\left(\frac{k_{sb}}{k_0}\right)^3-\frac{1}{3}\cdot\left(\frac{k_{sb}}{k_0}\right)^2+\frac{1}{2}\cdot\frac{k_{sb}}{k_0}\right)+\sqrt{\left(\frac{1}{27}\cdot\left(\frac{k_{sb}}{k_0}\right)^3-\frac{1}{3}\cdot\left(\frac{k_{sb}}{k_0}\right)^2+\frac{1}{2}\cdot\frac{k_{sb}}{k_0}\right)^2+\left(\frac{2k_{sb}}{3k_0}-\frac{1}{9}\cdot\left(\frac{k_{sb}}{k_0}\right)^2\right)^3}}+\sqrt[3]{\left(\frac{1}{27}\cdot\left(\frac{k_{sb}}{k_0}\right)^3-\frac{1}{3}\cdot\left(\frac{k_{sb}}{k_0}\right)^2+\frac{1}{2}\cdot\frac{k_{sb}}{k_0}\right)-\sqrt{\left(\frac{1}{27}\cdot\left(\frac{k_{sb}}{k_0}\right)^3-\frac{1}{3}\cdot\left(\frac{k_{sb}}{k_0}\right)^2+\frac{1}{2}\cdot\frac{k_{sb}}{k_0}\right)^2+\left(\frac{2k_{sb}}{3k_0}-\frac{1}{9}\cdot\left(\frac{k_{sb}}{k_0}\right)^2\right)^3}}$$

$$\phi_{c}=\frac{k_{c}}{3k_0}+\sqrt[3]{\left(\frac{1}{27}\cdot\left(\frac{k_{c}}{k_0}\right)^3-\frac{1}{3}\cdot\left(\frac{k_{c}}{k_0}\right)^2+\frac{1}{2}\cdot\frac{k_{c}}{k_0}\right)+\sqrt{\left(\frac{1}{27}\cdot\left(\frac{k_{c}}{k_0}\right)^3-\frac{1}{3}\cdot\left(\frac{k_{c}}{k_0}\right)^2+\frac{1}{2}\cdot\frac{k_{c}}{k_0}\right)^2+\left(\frac{2k_{c}}{3k_0}-\frac{1}{9}\cdot\left(\frac{k_{c}}{k_0}\right)^2\right)^3}}+\sqrt[3]{\left(\frac{1}{27}\cdot\left(\frac{k_{c}}{k_0}\right)^3-\frac{1}{3}\cdot\left(\frac{k_{c}}{k_0}\right)^2+\frac{1}{2}\cdot\frac{k_{c}}{k_0}\right)-\sqrt{\left(\frac{1}{27}\cdot\left(\frac{k_{c}}{k_0}\right)^3-\frac{1}{3}\cdot\left(\frac{k_{c}}{k_0}\right)^2+\frac{1}{2}\cdot\frac{k_{c}}{k_0}\right)^2+\left(\frac{2k_{c}}{3k_0}-\frac{1}{9}\cdot\left(\frac{k_{c}}{k_0}\right)^2\right)^3}}$$

By solving Eqs. (13)–(15), we can estimate the porosity and permeability distribution in the plastic zone and the mass of the produced sand, which can be obtained from the difference between the masses in the regions where porosity increased and decreased. To achieve this, the average permeability of the perforated sample at different flow rates and the mass of the produced sand are required. The following section describes the sand production experiments in which the proposed approach was applied.

3 Experimental results and discussions

3.1 High-pressure consolidation system for sand production experiments

In all existing experimental studies on sand production (Fattahpour et al., 2011, 2012; Nouri et al., 2006; Papamichos et al., 2001; Skjaerstein, Tronvoll, et al., 1997; van den Hoek et al., 2007; Wu & Choi, 2012), the sample was first prepared and then placed in the sand production apparatus, which may disturb the sample. In most cases, several samples were prepared before the test, and then tested in succession. The properties of the samples tested later may change over time, which affects the experimental results and reproducibility of the tests. The new apparatus designed for the sand production experiment allows the three processes of sandstone diagenesis, perforation, and fluid production to occur in the same sandstone specimen to minimize the disturbance of the sample, and replicates field conditions in the laboratory. The high-pressure consolidation system (HPCS) in Fig. 7 consists of a load frame (1) with a hydraulic actuator at the bottom (2), rails (3), a specimen cell (4), an actuator control unit (5), a data acquisition unit (6), a fluid pump (7), fluid pump valves (8), a controller (9), and a fluid tank (10). A large specimen (220 mm in height and 300 mm in diameter) was prepared and tested. The advantage of large specimens is that the boundary effects can be excluded in the experimental results.

The HPCS can apply a maximum axial vertical load of 5 000 kN, which is equivalent to a maximum reservoir depth of approximately 3 200 m. The servo-hydraulic mechanism inside the actuator (2) pushes the pedestal and the cell on top of it against the top cap and load frame. Thus, the axial load is applied by compressing the sample from the bottom. Stress or strain control modes can be activated depending on the test conditions.

The specimen is connected in series to the top cap, and the top plunger to the load frame at the top. A fluid flow of up to 5 L/min or under a maximum inlet pressure of 7 MPa can be injected through the eight inlet ports on the cell wall and/or two ports at the bottom (Fig. 8(a)). The outflow is made available through a central hole on the top cap to the inner space inside the top plunger, and to an outlet on the side of the plunger. The outlet pressure gauge and mass flowmeter are installed at the back end of the outlet tube (Fig. 8(b)), before the outlet valve and after the filter, to pass sand particles less than 0.4 mm and protect the transducer and flowmeter from large sand clusters. There are also additional valves for cleaning and bypassing purposes. Radial stress transducers and ultrasonic sensors are installed on the inner wall of the cell for direct contact with the specimen. The pore pressure transducer is located at the bottom of the specimen, and its surface is covered with filter paper to protect the piezoresistive element inside the transducer from sand particles.

The fluid pump unit and its valve station are used to distribute and control the flow of water and CO_2 (Fig. 9). The valve station has six valves: four for the radial ports and two for the top and bottom ports. The inlet tubing con-

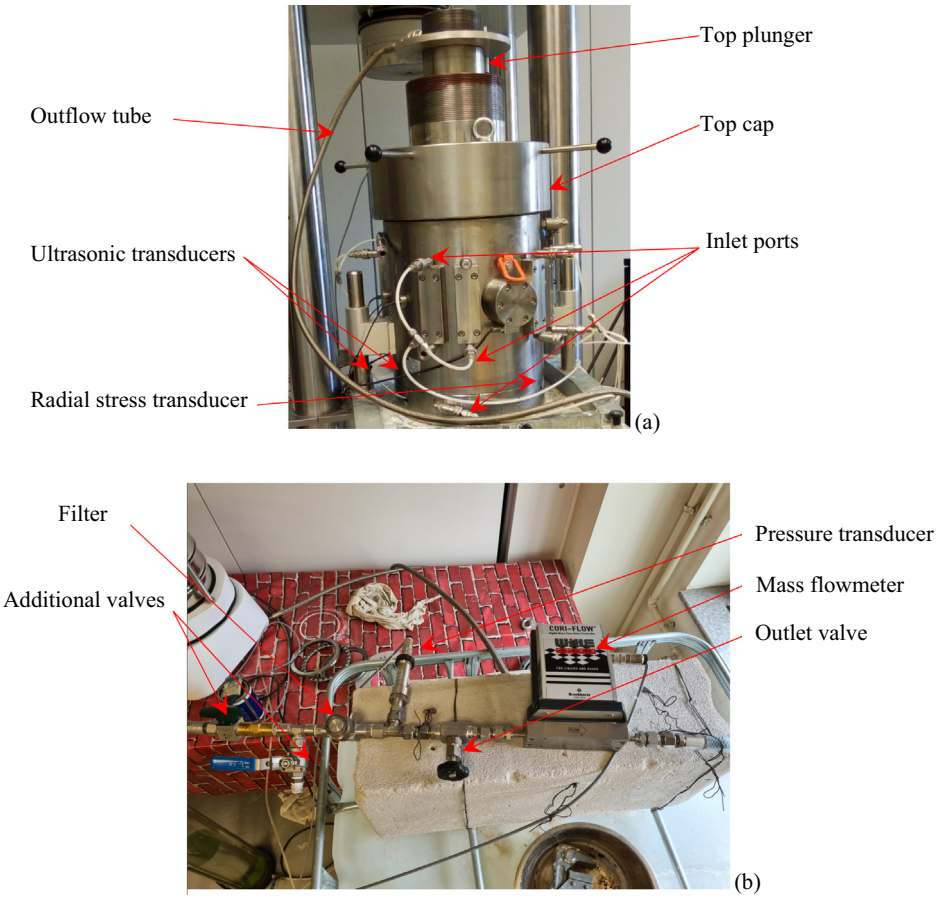

Fig. 8. High-pressure consolidation cell.

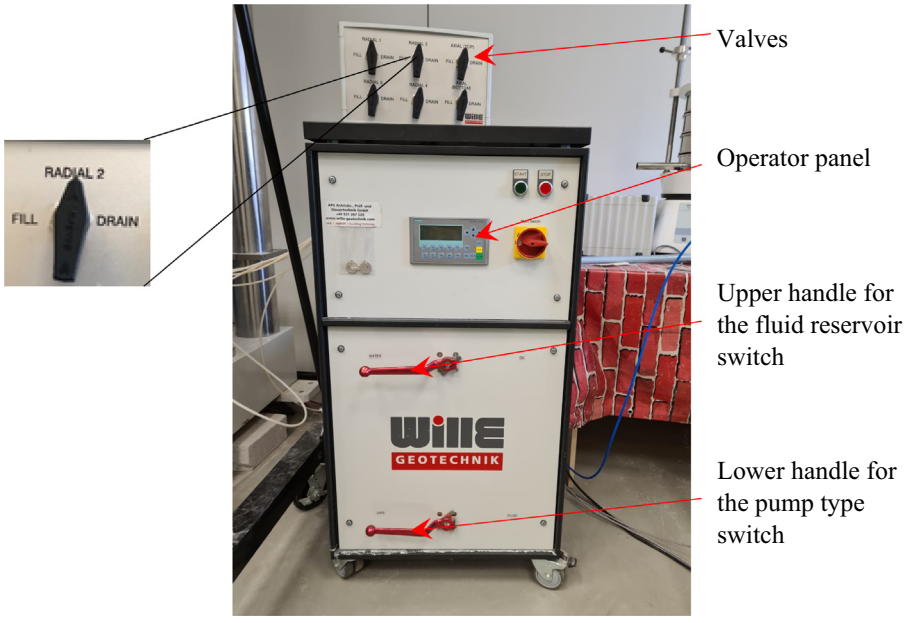

Fig. 9. Fluid pump unit and its valve station.

nects the valve station to the inlet ports. The vertical position of the valves indicates the closed condition. The fluid flows into the cell when the valve is on the "FILL" position and flows out of the cell when the valve is in the "DRAIN" position. The fluid pump can be controlled via software or manually using the operator panel on the pump. The soft-

ware allows the control of both the fluid rate and inlet pressure, while only the flow rate can be set using the operator panel. The fluid pump unit can be connected to two reservoirs with different fluids. The upper red handle is used to switch between reservoirs. In the present study, only water was injected; hence, the upper handle was turned to the left. The lower red handle is used to select the fluid injection method. When it is turned to the right, the pump is used; when turned to the left it connects to an outer pressure source. Thus, when we injected CO_2 from the pressurized gas balloon, the lower red handle was turned to the left; when we injected water, it was turned to the right.

Artificial sandstones were used in this study because of the difficulty in extracting the required number of samples from the weak sandstone reservoir. Artificial specimens were prepared to match the reservoir sandstone in terms of particle size distribution, mineralogy, strength, porosity, and permeability. The cementation method from Kozhagulova et al. (2018) was adopted, in which a 10% sodium silicate solution reacted with CO_2 to form cement bonds, and commercial sand was used as the sand material. Sandstone diagenesis was simulated in the laboratory as follows. For a 10% sand/cement ratio, we mixed 23 kg of quartz sand with a 2.3 kg sodium silicate solution, and then placed the mixture in the HPCS cell in three layers. Before placing the sample, the inner surface of the cell and the bottom plate were covered with filter paper to protect the inlet ports from sand particles. The top of each layer was scratched before adding the next layer to reduce the bedding effect. Afterwards, the top cap was installed. The top cap consists of two parts (Fig. 10): an inverted T-shaped loading column and a coupler with internal threads resting on the base of the loading column. The base of the loading column ensures uniform axial deformation of the sample. The upper part of the cell has external threads, on which the coupler of the top cap is screwed. Thus, the loading column was secured on top of the sample and sufficient water sealing was achieved.

A mobile overhead crane was used to navigate the top cap. The mass of the hooked top cap was regulated by the scale and spring to reduce the load on the threads; otherwise, the heavy mass of the top cap could damage the threads.

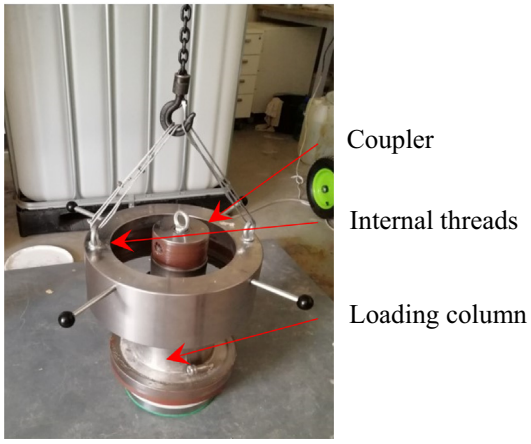

Fig. 10. Top cap.

Once the top cap was placed, the cell was rolled under the frame. We started lifting the cell at a rate of 5 mm/min in the displacement control mode until there was a 2–3 mm gap between the top plunger and the frame. Then, we switched to the stress control mode at 5 kPa/min up to the required vertical stress; the stress was maintained for 12 h to complete the consolidation. A low stress rate allowed us to observe the point at which the top plunger touched the frame and the sample was subjected to axial stress. This corresponds to the point at which the radial stress started to increase. The difference between the displacement value at this point and that at the end of consolidation was used to calculate the axial strain during consolidation. In addition, the sample porosity was estimated from the final sample dimensions and the total mass of the sand-cement mixture. The low stress rate also enables slow and uniform consolidation. Once the consolidation was completed, CO_2 was injected into the sample and allowed to circulate for 20 min at 0.5 MPa to activate the chemical process of cementation and create the artificial sandstone. This consolidation stress was kept constant at all stages except perforation.

The sample was saturated by flushing it with water from the bottom to the top at a constant inlet pressure of 50 kPa for 24 h. The inner surface of the cell was covered with filter paper so that the radial flow was uniformly distributed. The top surface of the sample was in tight contact with the top cap; hence, it was easier for water to flow through the sample rather than under the top cap. The flow rate was sufficiently high to defy gravity; hence, water did not flow to the bottom of the sample. The flow rate during flushing was used to calculate the initial permeability of the intact sample, assuming an isotropic condition. Darcy's equation for water flow through a porous cylindrical sample can be written as

$$q_w = \frac{-kA\Delta p}{\mu L}, \tag{18}$$

where q_w is the water flow rate at the inlet pressure of 50 kPa, A is the cross-sectional area of the sample, μ is the water viscosity, L is the sample height, $\Delta p = 50$ kPa is the applied drawdown when the inlet pressure is 50 kPa and the outlet is open to the atmosphere, and k is the permeability of the sample.

After the saturation stage, the specimen was unloaded and moved out of the loading position (using the supporting frame (3)), and a perforation tunnel was created by drilling a cylindrical hole with a diameter of 14 mm at the center of the top surface with the top cap in place. Figure 11 shows the sample surface before cementation, after cementation, and after perforation, respectively.

The sample was then returned to the loading position, and the consolidation stress was re-applied to the sample. This time, the stress rate was set to the higher value of

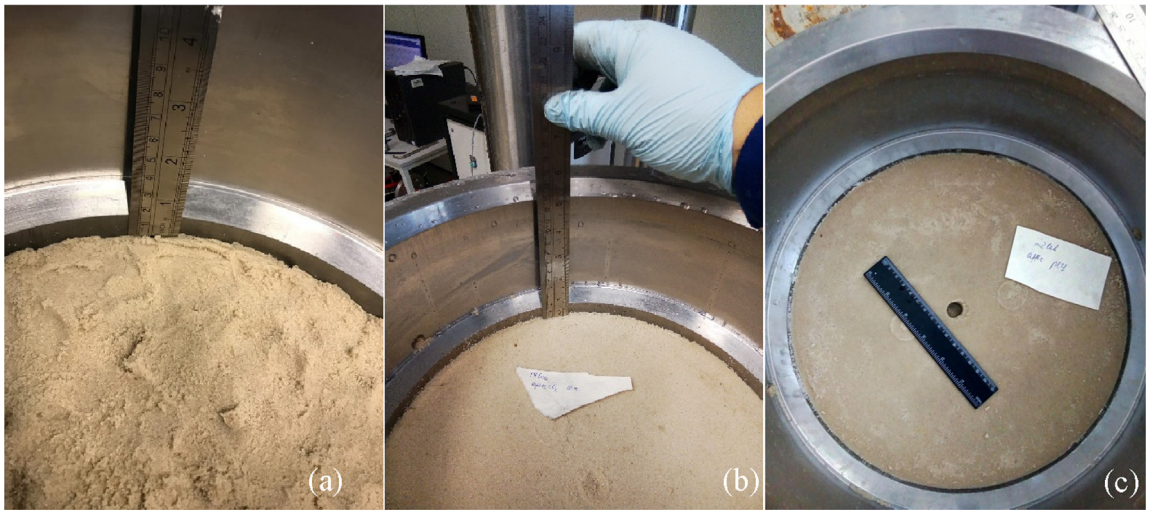

Fig. 11. Sample surface (a) before cementation; (b) after cementation; and (c) after perforation.

50 kPa/min, which did not affect the sample properties as it had already been compressed to the consolidation stress value. Once the target stress value was reached, a vertical flow was applied to remove the perforation debris. Some debris appeared at the outlet at 0.9 L/min. However, a minimum flow rate of 2 L/min flow rate was required for the debris to be completely washed out of the sample. The total mass of the debris was estimated from the dimensions of the hole, which is 52 g for D_I (inner diameter) = 14 mm.

Sand production experiments were conducted on the perforated sample using the flow diagram shown in Fig. 12. The cemented sample confined inside the cell from the previous steps was compressed vertically to the target stress value. Radial flow occurred as water was injected from the sides of the sample. Water and sometimes sand were observed to flow from the outlet of the top plunger to the sieve and high-accuracy scale system that filters and measures the amount of sand particles in the flow. The data on produced sand were recorded until a steady state was achieved for the liquid flow and sand production waned. The cleaned water was returned to the fluid tank for further circulation.

3.2 Sand production experimental results

The intact sample was characterized by an initial porosity and permeability of 38% and 207 mD, respectively. The experiments were conducted under axial stresses of 1–5 MPa. The tests attempted to replicate transient sand production in the field. For a specific drawdown pressure and the corresponding flow rate, an initial sand burst was observed followed by a gradual decrease in the sand rate toward a negligible value. A subsequent increase in the flow rate could trigger another smaller burst of sand production, which eventually waned. For each drawdown pressure in the laboratory, transient flow occurred during approximately the first 10 min, followed by another 30 min of steady-state flow. At each stress stage, different drawdown pressures were applied (Table 1). To apply a drawdown pressure, the inlet pressure was first increased to the required value by controlling the pump unit, while the outlet valve was closed. The no-flow condition was maintained to stabilize the fluid pressure until the outlet pressure sensor showed the same value as the inlet pressure; then, the outlet valve was opened to activate the flow. The flow

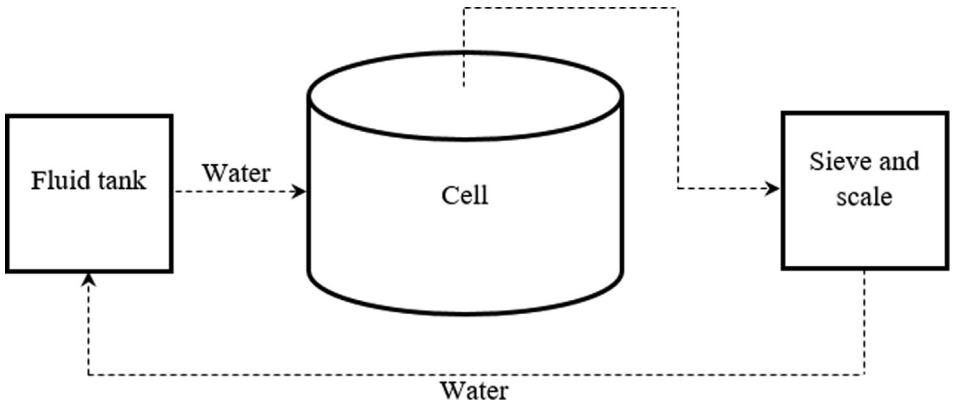

Fig. 12. Flow diagram of the sand production experiment.

Table 1
Sand production experimental results.

Test stages	Axial stress (kPa)	Radial stress 1 (kPa)	Radial stress 2 (kPa)	Drawdown (kPa)	Flow rate (L/min)	Average permeability (D)	Coefficient n (min/L)	Sand mass (g)
C1	1 000	485	481	200	0.90	0.178	0.14	0
				400	1.56	0.157	0.14	0
				600	2.04	0.144	0.14	52
				800	3.00	0.120	0.14	0
C2	2 000	696	1 100	400	1.63	0.155	0.14	0
				800	2.70	0.128	0.14	0
C3	3 002	1 000	1 505	800	2.50	0.120	0.16	0.854
				1 000	2.87	0.108	0.16	0.585
C4	4 000	1 270	1 625	800	2.36	0.112	0.20	6.652
				1 000	2.76	0.099	0.20	3.254
C5	5 003	1 589	1 940	1 200	2.70	0.084	0.26	6.031
				1 400	2.93	0.075	0.26	5.560

was maintained for approximately 40 min until no sand was observed. Perforation debris (52 g) was collected in the first stage C1 using a minimum lifting flow rate of 2 L/min. No additional sand was observed under axial stresses of 1 MPa and 2 MPa. On the contrary, sand was produced under stresses of 3 MPa, 4 MPa, and 5 MPa (Table 1).

The average permeabilities at stages C1 and C2 were calculated by Eq. (11) for the known drawdown and flow rate values, which are plotted in Fig. 13.

Figure 14 shows that the average permeability of the sample continuously declines as the flow rate increases. According to the Eq. (11), the average permeability value was affected by the fluid viscosity, sample dimensions, and hole radius. However, the sample radius and fluid viscosity did not change during the experiment. The sample contraction due to axial stress was negligible. The size of the central hole did not increase because no sand production was observed in these stages. These results indicate that the only reason for the decrease in average permeability is the formation of a low-permeability layer in the plastic zone next to the hole wall. The average permeability k_{avg} of the perforated sample is plotted as a function of the flow rate in Fig. 16.

The linear relationships in Fig. 14 can be approximated by the following linear equation:

$$k_{avg} = k(1 - nq), \tag{19}$$

where k_{avg} is the average permeability of the sample, k is the permeability of intact zone, q is the flow rate, and n is the proportionality coefficient. Because the unit of permeability is mD and that of the flow rate is L/min, the proportionality coefficient n is given in terms of min/L. If required by subsequent calculations, the coefficient n can be converted into s/cm^3 for consistency with other parameters. Experimental data from Shabdirova et al. (2020) suggest that the proportionality coefficient is a function of the applied stresses and strength of the sample, and increases with the intact permeability of the sandstone. If the permeability can be considered as an indicator of the rock strength, then n is higher for weaker rocks and higher applied stresses.

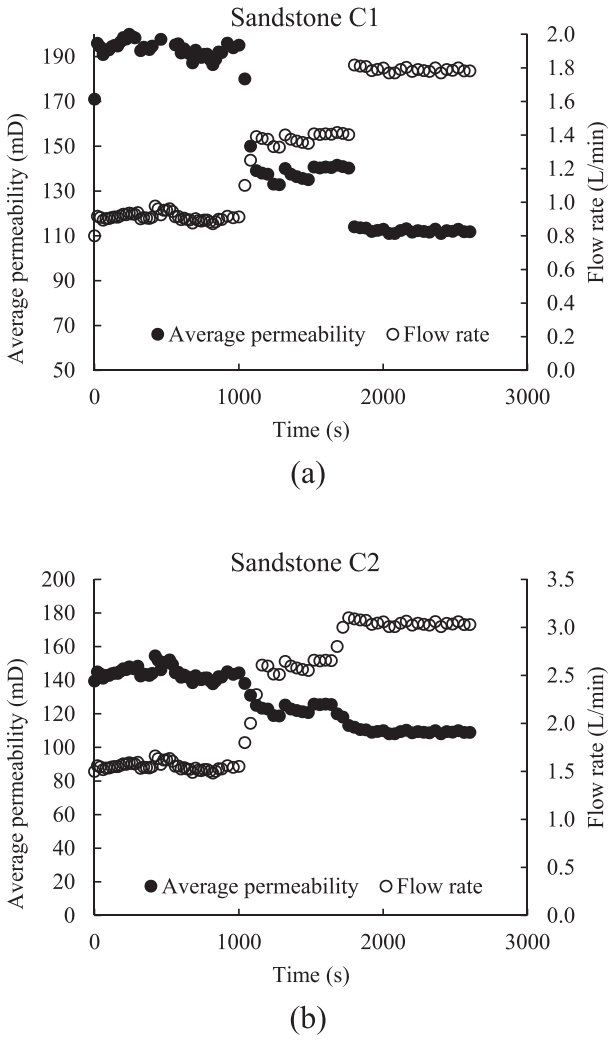

Fig. 13. Radial flow experimental results.

Knowledge of the value of the average permeability as a function of the flow rate in Eq. (15) and utilizing the equations of the shear failure model and the flow model enable

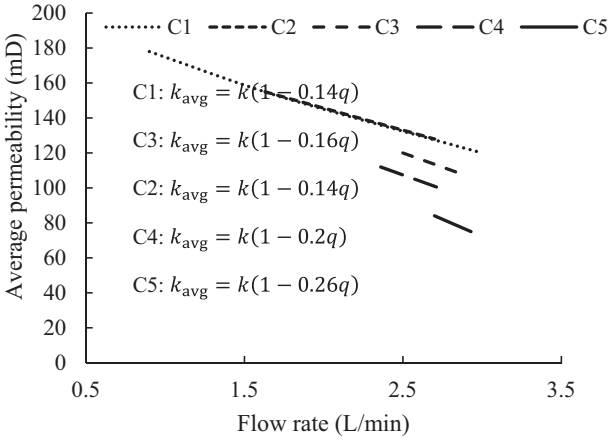

Fig. 14. Average permeability in sand production experiments.

the calculation of plastic zone properties for different drawdown and flow rate values. First, we recorded the drawdown and flow rate values in the steady state from the experiment. Then, we used Eq. (11) to calculate the average permeability. Afterwards, we solved the system of two equations (Eqs. (9) and (10)) to obtain the two unknowns k_p and R_p. Here, k_p is the average permeability of the plastic zone, which consists of a high-permeability shear band zone and a compaction zone.

The plastic zone permeability was calculated with various flow rate values using the model; the results are shown in Fig. 15. The symbols represent the data points of the real experiments and actual measured flow rates. The lines represent the full range of the model's prediction behavior, in which the plastic zone permeability was calculated using the assumed flow rate values outside the experimental range. For all stress levels and with an increasing flow rate, the plastic zone permeability decreased to a minimum value before increasing again at higher flow rate.

The sand production observed in the experiment must satisfy two conditions. First, material failure should occur, producing particles that are weakly connected to the matrix, and hence prone to hydrodynamic erosion. Second, the fluid energy must be sufficient to transport the detached particles to the outlet. Although the flow rate was higher than the minimum lifting flow rate of 2 L/min, no sand was collected in experiments C1 and C2; however, at the same flow rates, sand was produced in experiments C3, C4, and C5. This implies that both conditions are necessary for sand production. Furthermore, sand production in Fig. 15 occurred with the increase in plastic zone permeability (solid points).

This is consistent with the discussion in Fig. 6, which associated sand production with sand migration from the compaction zone to the shear band zone and perforation hole.

Now, we will analyze the experimental results in terms of porosity change in the plastic zone. We examined the experimental results for C3 (Table 1) at 800 kPa drawdown. Table 2 lists the input parameters for the volume and sand rate calculations.

We assumed that the maximum contraction occurred when the plastic zone permeability reached the minimum value of 61 mD according to Fig. 17. This corresponds to state A, which describes the porosity and permeability distribution before sand production for sandstone C3 at a drawdown pressure and a flow rate of 580 kPa and 2.1 L/min, respectively. State B shows the porosity and permeability distribution after sand production at 800 kPa drawdown pressure, where $k_p = 65$ mD is the average value of the permeability across the plastic zone, as in Eq. (13).

The k_0 value was obtained from the Kozeny–Carman relationship for the intact porosity and permeability values, shown as follows:

$$207\,\text{mD} = k_0 \frac{0.38^3}{(1-0.38)^2} \quad \Rightarrow \quad k_0 = 1.449.$$

Solving Eqs. (13)–(17) for the experimental results of sandstone C3, we can estimate the porosity distribution at states A and B (Tables 3 and 4).

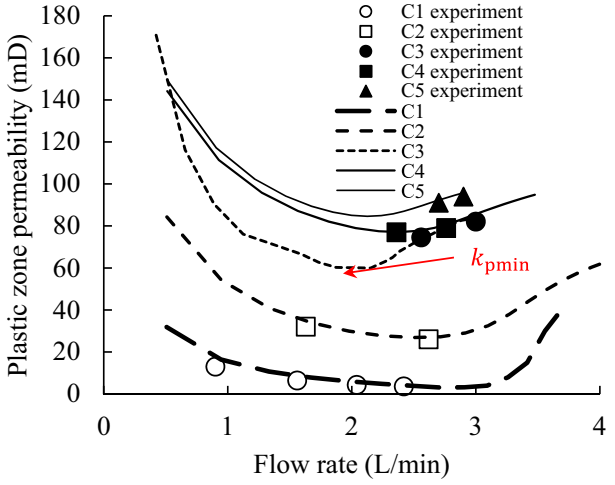

Fig. 15. Plastic zone permeability results.

Table 2
Input parameters for the model calculations under 3 MPa axial stress.

Parameter	Value
Inner hole radius (m)	0.007
Outer radius (m)	0.15
Drawdown (Pa)	800 000
Fluid viscosity (Pa•s)	0.001
Vertical stress (Pa)	3 000 000
Horizontal stress (Pa)	1 200 000
Flow rate (m^3/s)	4.21×10^{-5}
Intact zone permeability (m^2)	0.207×10^{-12}
Average permeability (m^2)	0.120×10^{-12}
Permeability coefficient	1.449
Cohesive strength of the sample (Pa)	120 000
Failure angle (°)	64
Sample height (m)	0.214
Sample diameter (m)	0.15

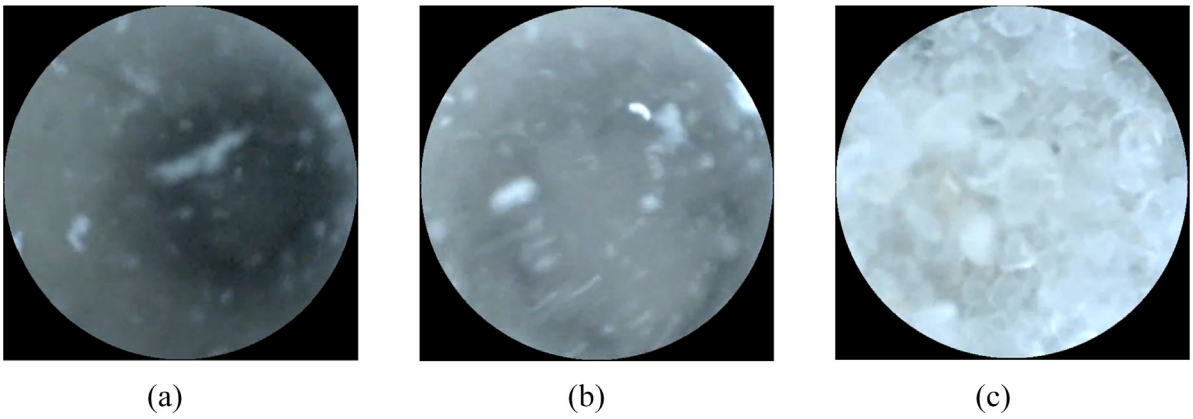

Fig. 16. Sand particles accumulated at the bottom of the hole captured at different heights: (a) from the top part of the hole; (b) from the middle part of the hole; and (c) from the bottom of the hole.

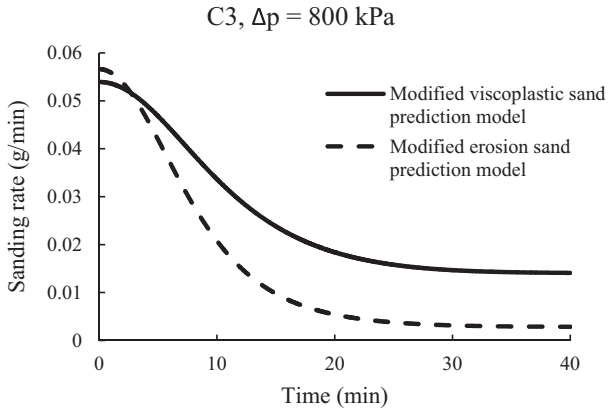

Fig. 17. Results of transient sand prediction model for sample C3 at 800 kPa drawdown.

In the case where some sand was trapped in the shear band zone during the transport from the compaction zone to the hole, the porosity in the shear band zone decreased, and only a portion of the transported sand was produced. In this case, the mass of sand produced is dependent on the amount of sand trapped in the shear band zone (Table 4).

The experimental results show that 0.854 g of sand was produced at 2.5 L/min during the first 10 min. The experiment was stopped after 40 min as no more sand was observed. On the other hand, Table 4 shows that we could have produced a maximum of 14 g sand, which suggests a missing time column in Table 4. Thus, 10 min is required for the fluid flow to transport sand particles from the compaction zone to the shear band zone to increase porosity from 0.23 to 0.54, and transport 0.8 g of sand to the perforation hole. The fact that we did not observe sand for the remaining 30 min indicated that the subsequent sand migration was very slow, and we stopped the experiment before producing all the producible sand predicted by the model, i.e., 14 g. The continuous sand measurement technique could be a solution to this problem in future studies; however, in the present study, the sand was not measured continuously. The microcamera pictures taken inside the hole after the test indicated that some sand particles accumulated at the bottom of the hole (Fig. 16). This may be due to the slippage of detached single particles into larger clusters; hence, the applied flow rate was insufficient to lift them to the surface.

Table 3
Model results for state A.

R_{sb}^{A} (m)	R_{p}^{A}(m)	ϕ_{sb}^{A}	k_{sb}^{A}(mD)	ϕ_{c}^{A}	k_{c}^{A}(mD)	ϕ_{p}^{A}	k_{p}^{A}(mD)	q(L/min)
0.010 4	0.013 7	0.584	1 668	0.232 8	31	0.279 6	61	2

Table 4
Model results for state *B*.

R_{sb}^{B} (m)	R_{p}^{B}(m)	ϕ_{sb}^{B*}	k_{sb}^{B}(mD)	ϕ_{c}^{B}	k_{c}^{B}(mD)	ϕ_{p}^{B}	k_{p}^{B}(mD)	q(L/min)	m_{s}^{min}
0.016	0.019 4	0.536	1 038	0.201 8	18.7	0.284 4	65	2.5	0.3
0.016	0.019 4	0.537	1 048	0.201 8	18.7	0.284 4	65	2.5	0.5
0.016	0.019 4	0.538	1 060	0.201 8	18.6	0.284 4	65	2.5	0.8
0.016	0.019 4	0.54	1 078	0.201 7	18.6	0.284 4	65	2.5	1.4
0.016	0.019 4	0.545	1 138	0.201 6	18.6	0.284 4	65	2.5	3
0.016	0.019 4	0.556	1 268	0.201 3	18.5	0.284 4	65	2.5	6
0.016	0.019 4	0.577	1 558	0.200 9	18.4	0.284 4	65	2.5	12
0.016	0.019 4	0.584	1 668	0.200 8	18	0.284 4	65	2.5	14

According to the model, R_i did not change until the porosity at R_i exceeded 1. For the flow rates considered, the calculations showed that the porosity increased near the hole but did not reach 1; therefore, R_i did not change.

3.3 Transient sand production prediction

The new findings on the porosity and permeability distribution discussed above will be used to modify the existing transient sand production prediction models and demonstrate the importance of plastic zone properties. The first model proposed by Geilikman et al. (1994) and extended by van den Hoek and Geilikman (2003) considered sand production as a viscoplastic granular flow. The model stated that sand was produced in the plastic zone around a hole, and this plastic zone had a higher porosity than the intact zone owing to sand production. The second model is based on the studies by Vardoulakis et al. (1996), Skjaerstein, Stavropoulou, et al. (1997), and Papamichos et al. (2001) on the erosion behavior of solids due to fluid flow. The authors introduced a sand production coefficient λ to describe the erosion behavior of the sand matrix. In the original model (Papamichos et al., 2001), sand was produced in the intact zone, and the intact zone porosity was used as the initial porosity value in the calculations.

We have shown above that the plastic zone has lower permeability and porosity compared with the intact zone and consists of two subzones: a high-permeability shear band zone and a low-permeability compaction zone. On the basis of our findings, we modified the models proposed by van den Hoek and Geilikman (2003) and Papamichos et al. (2001) in terms of the plastic zone radius, permeability, and porosity. Thus, we propose that sand is produced in the compaction zone when its porosity and permeability increase from ϕ_c^A to ϕ_{sb}^B and from k_c^A to k_{sb}^B, respectively, and the plastic zone radius changes from R_{sb}^A to R_{sb}^B.

The sanding rate was calculated using the two modified models and compared with the experimental results under the axial stress of 3 MPa and the drawdown pressure of 800 kPa. Table 5 presents the input parameters for the sanding rate calculations, while Fig. 17 shows the model results.

As shown in Fig. 17, the peak rates from the results of the modified models are comparable. However, the tail of the curve is far above zero for the modified viscoplastic sand prediction model. The total sand mass produced during the first 40 min can be estimated by calculating the area under the sanding rate curve: $m_s^{\text{viscoplastic}}(40) = 1$ g for the modified viscoplastic model and $m_s^{\text{erosion}}(40) = 0.588$ g for the modified erosion model. Both results are greater than the sand mass produced during the experiment. At this calculated sanding rate, the modified viscoplastic model and the modified erosion model would require 16 h and 83 h, respectively, to produce all the theoretically producible sand mass (14 g).

For a clearer view of the model performance, we conducted all calculations in the previous and current sections for all experiments. Table 6 shows the calculation results of all the experiments.

Table 6 shows that the modified sanding rate prediction models tended to underestimate the produced sand mass. The relative error reached as high as 57%, while the lowest value ranged between 2% and 8%. For each model, we used the same coefficients (e.g., formation viscosity or sand production coefficient) as the original model. However, these constants may not be applicable to our sample, which may result in larger errors. To estimate the significance of the modification based on the plastic zone properties, we

Table 5
Input parameters for the calculations of sanding rate under 3 MPa axial stress.

Parameter	Notation	Value
Initial radius of the shear band zone (m)	R_{sb}^A	0.010 4
Outer radius (m)	R_o	0.15
Current radius of the shear band zone (m)	R_{sb}^B	$R_{sb}^A + 0.0055 \cdot (1 - e^{-\frac{t^2}{10^6}})$
Drawdown (Pa)	$\Delta p = p_o - p_i$	800 000
Fluid viscosity (Pa·s)	μ	0.001
Effective radial stress at hole wall (Pa)	σ_i	0
Radial stress at infinity (Pa)	σ_∞	1 200 000
Compaction zone permeability before sand production (m^2)	k_c^A	0.031×10^{-12}
Compaction zone permeability after sand production (m^2)	k_{sb}^B	1.668×10^{-12}
Compaction zone porosity before sand production	ϕ_c^A	0.23
Compaction zone porosity after sand production	ϕ_{sb}^B	0.58
Intact zone UCS (MPa)	UCS_i	1
Plastic zone UCS (MPa)	UCS_p	0
Friction angle (°)	ϕ	38
Dilatancy angle (°)	ψ	8
Viscoplastic viscosity (Pa·s)	η	10^{11}
Sand production coefficient (m^{-1})	λ	3×10^{-5}–3×10^{-4}
Poroelastic coefficient	γ_p	0.9
Sample height (m)	L	0.214

Table 6
Experimental and modeling results of the sand production.

Axial stress (MPa)	Drawdown (kPa)	Sand mass from the experiment (g)	Theoretical total sand mass (g)	The modified viscoplastic model			The modified erosion model		
				Sand mass in 40 min (g)	Relative error (%)	Time to produce all sand (h)	Sand mass in 40 min (g)	Relative error (%)	Time to produce all sand (h)
3	800	0.854	14	1.006 8	15	16	0.588	45	83
3	1 000	0.585	43	0.4	46	27	0.573	2	238
4	800	6.652	36	5.890 1	13	5	4.25	57	20
4	1 000	3.254	130	3.023	8	55	4.1	21	81
5	1 200	6.031	143	5.324 3	13	43	5.65	7	61
5	1 400	5.56	148	4.560 2	22	38	5.3	5	63

compared the relative error of the original models by van den Hoek and Geilikman (2003) and Papamichos et al. (2001) with the current modified models. As it can be seen in Table 7, the performance of the modified models is better than that of the original models, despite their moderate-to-high error values. The original models predicted sand masses 2–3 times greater than those in the experiment. The porosity ranged from 0.38 to 0.6 in the original models; in the modified models, it ranged from 0.2 to 0.6; as it can be seen, the difference is not very large. However, the change in the plastic zone radius was significantly different in the original and modified models. Therefore, the plastic zone properties should be accurately defined for better predictions.

To further assess the modified models, the sanding rate data from the weak sandstone reservoir were used. The following section presents the field validation results of the modified viscoplastic model, which is more convenient to adapt for field conditions compared with the modified erosion model.

3.4 Field data validation

The sand data obtained from a heavy oil sandstone reservoir in Kazakhstan were used to validate the sand production model with updated zone properties. The assumptions of the model were applied to wells that met the following criteria:

(1) The well produces from a single or a couple of homogeneous production layers.
(2) The thickness of the producing layer is greater than 2 m.
(3) The pay-to-gross ratio of the producing layer should exceed 80%.
(4) The water cut of the produced liquid is less than 10%.

As the model was developed for different production stages with a constant flow rate, the following criterion was added:

(5) The well produces at an approximately constant flow rate.

After screening 3 000 production wells from the field, 40 wells that satisfied all the above conditions were chosen to validate the model. The field data includes the average values of the fluid rate, sand rate, and bottom-hole pressure per month. The comparison of the model and field data was conducted in terms of the magnitude of the peak sand production rate and the pattern of sanding behavior.

The prediction for a specific well producing from horizon B is explained in detail as an example. The effective thickness of the interval is 2.9 m at a depth of 235 m. The vertical stress at the outer boundary is $\sigma_v = 5.3$ MPa at 221 m. The horizontal stress at the outer boundary is $\sigma_H = \sigma_h = 0.4 \cdot \sigma_v = 2.12$ MPa. The current reservoir pressure is 2 MPa, and the bottom-hole pressure is 0.77 MPa.

The model used in this study was developed for a vertical cavity. For the horizontal perforation of a vertical well, the stress distributions can be modified by transformation formulas (Fjaer et al., 2008) for the application of the

Table 7
Comparison between the original models (Papamichos et al., 2001; van den Hoek & Geilikman, 2003) and the modified models (current study).

Axial stress (MPa)	Drawdown (kPa)	Sand mass from the experiment (g)	Relative error (%)			
			Viscoplastic model	Modified viscoplastic model	Erosion model	Modified erosion model
3	800	0.854	185	15	73	45
3	1 000	0.585	193	46	78	2
4	800	6.652	122	13	56	57
4	1 000	3.254	81	8	58	21
5	1 200	6.031	202	13	104	7
5	1 400	5.56	178	22	106	5

model. The sand rate was calculated for a single perforation tunnel, and the total sand rate of the well was determined by multiplying the result by the number of perforations. The same geometry was assumed in the calculations for a single perforation, as the perforation procedure was identical throughout the field, with a density of 16 shots per meter and a phasing of 90°. This implies that the vertical distance between two adjacent horizontal perforations is 0.25 m. The half-distance between adjacent perforations was taken as an outer boundary, i.e., $R_o = 0.125$ m. The gun passport suggests the average diameter and length of the perforation tunnel as $2R_i = 0.016\ 6$ m and $L = 2$ m, respectively.

The field data on the porosity and permeability for this well are unavailable. However, the values for horizon B are in the following ranges: the porosity of 0.31–0.39 and the permeability of 89–1 050 mD. The initial porosity and permeability of the field were assumed to be the same as those in the sand production experiments: 0.38 and 207 mD, respectively. Similarly, as the cohesion and friction angle of the reservoir rock are unknown, they were assumed to be 0.12 MPa and 64°, respectively, as those in the experiment. All the input data are listed in Table 8.

The production of the well was approximately 7.5 t/d for 36 months with a water cut below 10%. The comparison of the associated sand rate of the well and the predicted values in Fig. 18 show that the model captured the peak sand rate and the cessation of sanding in the steady state. However, the field data changed gradually with persistent fluctuations. The main questions that the prediction model should answer are how much sand will be produced at the peak of sand production, and how long this peak will last so that the surface facilities can be arranged accordingly to handle the produced sand. Therefore, the model performance can be considered as satisfactory and provides valuable information.

Similar calculations were conducted for all 40 wells producing from five horizons: A1, A2, B, G, and V. Because of the specific structure of the field, the producing depths of the horizons ranged from 260 m to 530 m; the exact numbers are known for each well. As in the experiments, single values of the cohesion and friction angle, porosity, and permeability were used for all 40 wells. The perforation characteristics were assumed to be the same for all wells; however, the number of perforations varied depending on the thickness of the production interval.

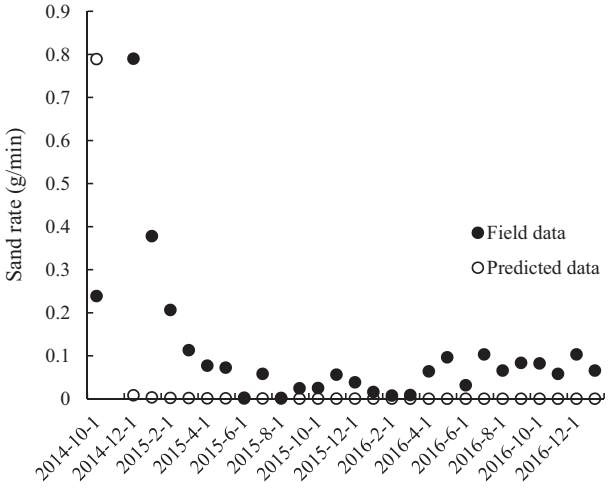

Fig. 18. Field data validation of the model.

Figure 19 shows the model performance in the prediction of the peak sand rate for all 40 wells. The ordinate indicates the number of wells in which the prediction falls within a particular error range. The error was calculated as the ratio of the predicted maximum rate to the maximum field rate. If the ratio is higher than the unit, then the model overpredicts by the amount above one multiplied by 100. If the ratio is less than one, then the model underpredicts the difference between the ratio and one multiplied by 100.

The peak sand rates of eight out of the total 40 wells were predicted within a 20% error, which is considered a sufficient level of accuracy. Most wells were predicted with errors within 20%–40% of the actual data. The eight wells produced from horizon B in the central part of the field. This is the same horizon that the well in Fig. 18 produced from, where the reservoir pressure did not exceed 2 MPa. The results suggest that the material and fluid properties used in the model are the most applicable to this location.

Table 8
Input data for field validation. A well produced from horizon B, the central part.

	Parameter	Unit	Value
Pressures	Fluid pressure at the outer boundary, p_o	MPa	2
	Fluid pressure at the borehole, p_w	MPa	0.77
	Vertical stress at the boundary, σ_v	MPa	5.3
	Maximum and minimum horizontal stresses at the boundary, $\sigma_H = \sigma_h$	MPa	2.12
	Depth	m	235
Perforation dimensions	Perforation radius, R_i	m	0.008 3
	Perforation length, L	m	2
	Outer boundary radius, R_o	m	0.125
	Number of perforations, N		46
Fluid properties	Fluid rate	t/d	7.5
	Fluid viscosity	Pa·s	0.55

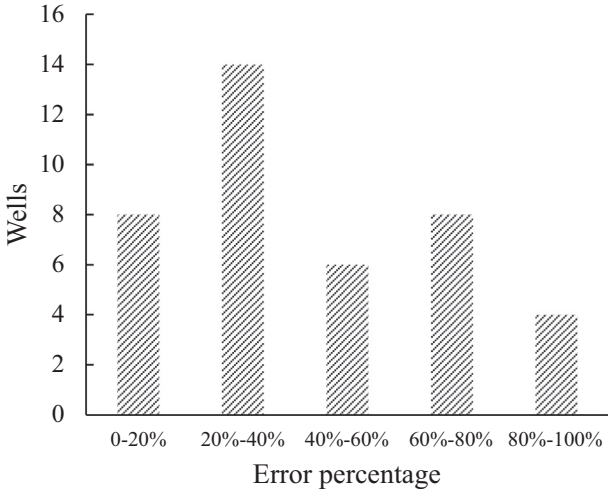

Fig. 19. The model performance for 40 wells.

However, the field conditions may vary for both the reservoir rock and fluid properties; these were not considered in the predictions for the 40 wells.

4 Conclusion

This study analytically and experimentally investigated the role of plastic zone permeability and porosity in the prediction of the sand volume and rate. Large-scale sand production experiments were conducted using a customized HPCS. Existing sand prediction models were modified with new information on the plastic zone permeability to obtain a semi-analytical prediction model for sand production from a hollow cylinder weak artificial sandstone under radial flow. The model obtained was validated using sand data from a weak sandstone reservoir. The current study was conducted to demonstrate the importance of the plastic zone permeability and porosity distribution around a perforation hole. In weak sandstone, the plastic zone consists of two subzones: a high-permeability shear band zone and a low-permeability compaction zone. The average permeability and porosity in the plastic zone were lower than those in the intact zone. Existing sand prediction models can be updated with the plastic zone properties for improved performance. The results demonstrated the significance of the decreased plastic zone porosity and permeability in predicting sand production. The modified model exhibited a positive performance for further development and improvement in laboratory and real-world applications.

Declaration of Competing Interest

The authors declare that they have no known competing financial interests or personal relationships that could have appeared to influence the work reported in this paper.

Acknowledgments

Funding source: This research was sponsored by the Nazarbayev University (Grant No. OPCRP2022006). The authors would like to thank the operating company for providing the field data.

References

Al-Shaaibi, S. K., Al-Ajmi, A. M., & Al-Wahaibi, Y. (2013). Three dimensional modeling for predicting sand production. *Journal of Petroleum Science and Engineering, 109*, 348–363.

Araujo, E. F., Alzate, G. A., Arbelaez, A., Peña, S., Cardona, A., & Naranjo, A. (2014). Analytical prediction model of sand production integrating geomechanics for open hole and cased – perforated wells. *SPE heavy and extra heavy oil conference*. Society of Petroleum Engineers.

Arora, D. S., & Sharma, M. M. (2000). The nature of the compacted zone around perforation tunnels. *Proceedings - SPE International Symposium on Formation Damage Control, 10*, 113–124.

Bratli, R. K., & Risnes, R. (1981). Stability and failure of sand arches. *Society of Petroleum Engineers Journal, 21*(2), 236–248.

Carman, P. C. (1939). Permeability of saturated sands, soils and clays. *The Journal of Agricultural Science, 29*(2), 262–273.

Cerasi, P., Papamichos, E., & Stenebråten, J. F. (2005). Quantitative sand-production prediction: Friction-dominated flow model. *SPE Latin American and Caribbean Petroleum Engineering Conference*. June 20–23, 2005. Rio de Janeiro, Brazil.

Cuss, R. J., Rutter, E. H., & Holloway, R. F. (2003). Experimental observations of the mechanics of borehole failure in porous sandstone. *International Journal of Rock Mechanics and Mining Sciences, 40*(5), 747–761.

Daigle, H., Rasromani, E., & Gray, K. E. (2017). Near-wellbore permeability alteration in depleted, anisotropic reservoirs. *Journal of Petroleum Science and Engineering, 157*, 302–311.

Dake, L. (2008). Fundamentals of reservoir engineering. Developments in Petroleum Science. Elsevier Science B.V.

Fanchi, J. R. (2000). Integrated flow modeling. *Elsevier, 49*, 1–287.

Fattahpour, V., Moosavi, M., & Mehranpour, M. (2011). An experimental rock mechanics investigation for sand production in oil fields. *45th US Rock Mechanics/Geomechanics Symposium.*

Fattahpour, V., Moosavi, M., & Mehranpour, M. (2012). An experimental investigation on the effect of rock strength and perforation size on sand production. *Journal of Petroleum Science and Engineering, 86–87*, 172–189.

Fjaer, E., Holt, R. M., Horsrud, P., Raaen, A. M., & Risnes, R. (2008). *Petroleum related rock mechanics,* 2nd ed., Vol. 30. Elsevier B.V.

Fuh, G., & Morita, N. (2013). Sand production prediction analysis of heterogeneous reservoirs for sand control and optiaml well completion design. *International Petroleum Technology Conference*, March 26–28, Beijing, China.

Geilikman, M. B., Dusseault, M. B., & Dullien, F. A. (1994). Sand production as a viscoplastic granular flow. *SPE Symposium on Formation Damage Control.* February 7–10, 1994. Lafayette, Louisiana, USA.

Goshtasbi, K., Elyasi, A., & Naeimipour, A. (2013). Numerical assessment of the mechanical stability in vertical, directional and horizontal wellbores. *International Journal of Mining Science and Technology, 23*(6), 937–942.

Han, G., Dusseault, M. B., & Cook, J. (2002). Quantifying Rock Capillary Strength Behavior in Unconsolidated Sandstones. In *Proceedings of the SPE/ISRM Rock Mechanics in Petroleum Engineering Conference* (pp. 171–180).

Han, G., & Dusseault, M. B. (2003). Description of fluid flow around a wellbore with stress-dependent porosity and permeability. *Journal of Petroleum Science and Engineering, 40*(1–2), 1–16.

Han, G., Shepstone, K., Harmawan, I., Er, U., Jusoh, H., Lin, L. S., Pringle, D., Koya, R., Carney, S., Barker, L., Morita, N., Papamichos, E., Cerasi, P., Sayers, C., Heiland, J., Bruno, M., & Diessl, J. (2011). A comprehensive study of sanding rate from a gas field: From reservoir to completion, production, and surface facilities. *SPE Journal, 16*(2), 463–481.

Hayavi, M. T., & Abdideh, M. (2017). Establishment of tensile failure induced sanding onset prediction model for cased-perforated gas wells. *Journal of Rock Mechanics and Geotechnical Engineering, 9*(2), 260–266.

Holt, R. M. (1990). Permeability reduction induced by a nonhydrostatic stress field. *SPE Formation Evaluation, 5*(4), 444–448.

Kessler, N., Wang, Y., & Santarelli, F. J. (1993). A Simplified Pseudo 3D Model To Evaluate Sand Production Risk in Deviated Cased Holes. *SPE Annual Technical Conference and Exhibition*. October 3–6, 1993. Houston, Texas, USA. https://doi.org/10.2118/26541-ms.

Khamitov, F., Minh, N. H., & Zhao, Y. (2021). Coupled CFD–DEM numerical modelling of perforation damage and sand production in weak sandstone formation. *Geomechanics for Energy and the Environment, 28,* 100255.

Kozeny, J. (1927). Uber Kapillare Leitung des Wassers im Boden. Vienna: Royal Academy of Science (in German) (pp. 271–306). Vienna: Royal Academy of Science (in German).

Kozhagulova, A. A., Shabdirova, A. D. D., Tokazhanov, G., Minh, N. H. H., G., T., & Minh, N. H. H. (2018). Bond Characteristics of Artificial Sandstones with Sodium Silicate Cement. *52nd US Rock Mechanics/Geomechanics Symposium.* June 17–20, 2018. Seattle, Washington, USA.

Morita, N., Whitfill, D. L., Massie, I., & Knudsen, T. W. (2007). Realistic Sand-Production Prediction: Numerical Approach. *SPE Production Engineering, 4*(01), 15–24.

Nouri, A., Vaziri, H. H., Belhaj, H. A., & Islam, M. R. (2006). Sand-production prediction: A new set of criteria for modeling based on large-scale transient experiments and numerical investigation. *SPE Journal, 11*(02), 227–237.

Papamichos, E., & Furui, K. (2013). Sand production initiation criteria and their validation. In *In 47th US Rock Mechanics/Geomechanics Symposium* (pp. 198–206).

Papamichos, E., & Furui, K. (2019). Analytical models for sand onset under field conditions. *Journal of Petroleum Science and Engineering, 172*, 171–189.

Papamichos, E., Skjaerstein, A., & Tronvoll, J. (2000). A volumetric sand production experiment. *Pacific Rocks*, 303–310.

Papamichos, E., Vardoulakis, I., Tronvoll, J., & Skjaerstein, A. (2001). Volumetric sand production model and experiment. *International Journal for Numerical and Analytical Methods in Geomechanics, 25*(8), 789–808.

Raghavan, R., & Chin, L. Y. (2002). Productivity changes in reservoirs with stress-dependent permeability. *SPE Annual Technical Conference and Exhibition*, September 29–October 2, 2002. San Antonio, Texas, USA.

Risnes, R., Bratli, R. K., & Horsrud, P. (1982). Sand stresses around a wellbore. *Society of Petroleum Engineers Journal, 22*(06), 883–898.

Sarda, J.-P., Ferfera, F. M. R., Vincké, O., Boutéca, M., & Longuemare, P. (1988). Experimental study of the stress paths influence on monophasic permeability evolution. In *In Society of Core Analysts, International Symposium* (pp. 14–16).

Shabdirova, A. D., Khamitov, F., Kozhagulova, A. A., Amanbek, Y., Minh, N. H., & Zhao, Y. (2020). Experimental and numerical investigation of the plastic zone permeability. *54th U.S. Rock Mechanics/Geomechanics Symposium*, June 2020. Paper Number: ARMA-2020-1626.

Shabdirova, A., Minh, N. H., & Zhao, Y. (2019). A sand production prediction model for weak sandstone reservoir in Kazakhstan. *Journal of Rock Mechanics and Geotechnical Engineering, 11*(4), 760–769.

Skjaerstein, A., Stavropoulou, M., Vardoulakis, I., & Tronvoll, J. (1997). Hydrodynamic erosion; A potential mechanism of sand production in weak sandstones. *International Journal of Rock Mechanics and Mining Sciences, 34*(3–4), 292.e1–292.e18.

Skjaerstein, A., Tronvoll, J., Santarelli, F. J., & Joranson, H. (1997). Effect of water breakthrough on sand production: Experimental and field evidence. *Proceedings - SPE Annual Technical Conference and Exhibition*, 565–575.

Tovar, J., Salazar, A., & Salazar, N. (2007). Integrating drilling and geomechanical damage in sandstone reservoirs: Identification, quantification, and removal. *SPE - European Formation Damage Conference, Proceedings, EFDC, 1*, 330–337.

Tronvoll, J., & Fjær, E. (1994). Experimental study of sand production from perforation cavities. *International Journal of Rock Mechanics and Mining Sciences, 31*(5), 393–410.

van den Hoek, P. J., Hertogh, G. M. M., Kooijman, A. P., de Bree, P., Kenter, C. J., & Papamichos, E. (2007). A new concept of sand production prediction: Theory and laboratory experiments. *SPE Drilling & Completion, 15*(04), 261–273.

van den Hoek, P. J. & Geilikman, M. B. (2003). Prediction of sand production rate in oil and gas reservoirs. *SPE Annual Technical Conference and Exhibition*.

Vardoulakis, I., Stavropoulou, M., & Papanastasiou, P. (1996). Hydro-mechanical aspects of the sand production problem. *Transport in Porous Media, 22*(2), 225–244.

Wang, H., & Sharma, M. M. (2017). The role of elasto-plasticity in cavity shape and sand production in oil and gas wells. *SPE Annual Technical Conference and Exhibition*. October 9–11, 2017.San Antonio, Texas, USA.

Wang, Y., & Dusseault, M. B. (1996). Sand production potential near inclined perforated wellbores. In *47th Annual Technical Meeting of the Petroleum Society*. June 9–11, 1996. Calgary, Alberta, Canada.

Weingarten, J. S., & Perkins, T. K. (1995). Prediction of sand production in gas wells: Methods and Gulf of Mexico case studies. *Journal of Petroleum Technology, 47*(07), 596–600.

Wu, B., & Choi, S. K. (2012). Effect of mechanical and physical properties of rocks on post-failure post cavity development – experimental and numerical studies. *The 46th US Rock Mechanics/Geomechanics Symposium.* June 24–27, 2012. Chicago, Illinois, USA.

Wu, B., Mohamed, N., Tan, C., Sukahar, W., Viswanathan, C., & Yee, H. (2006). An integrated wellbore stability and sand production prediction study for a multi-field gas development. *In SPE Asia Pacific Oil and Gas Conference and Exhibition.* September 11–13, 2006. Adelaide, Australia.

Wu, B., Choi, S. K., Denke, R., Barton, T., Viswanathan, C., Lim, S., Zamberi, M., Shaffee, S., Fadhlan, N., Johar, Z., Jadid, M. B., & Madon, B. B. (2016). A new and practical model for amount and rate of sand production. *Offshore Technology Conference*. Malaysia: Kuala Lumpur.

Yan, M., Deng, J., Yu, B., Li, M., Zhang, B., Xiao, Q., & Tian, D. (2020). Comparative study on sanding characteristics between weakly consolidated sandstones and unconsolidated sandstones. *Journal of Natural Gas Science and Engineering, 76,* 103183.

Yi, X. (2003). *Numerical and Analytical Modeling of Sanding Onset Prediction* [Doctoral dissertation, Texas A&M University].

Zhu, W., & Wong, T. (1997). The transition from brittle faulting to cataclastic flow: Permeability evolution. *Journal of Geophysical Research: Solid Earth, 102*(B2), 3027–3041.